



## RESEARCH ARTICLE

10.1002/2015JC011510

## Mooring observations of equatorial currents in the upper 1000 m of the western Pacific Ocean during 2014

Fan Wang<sup>1,2</sup>, Jianing Wang<sup>1,2</sup>, Cong Guan<sup>1,3</sup>, Qiang Ma<sup>1,3</sup>, and Dongxiao Zhang<sup>4,5</sup>

## Key Points:

- ADCP measurements resolve time-depth variations of equatorial currents in western Pacific Ocean.
- Observed intraseasonal variations of equatorial currents at 50–1000 m with periods of 37–73 days
- During fickle El Niño of 2014, NECC was at its southernmost position and weakest over past 20 years

## Correspondence to:

F. Wang,  
fwang@qdio.ac.cn

## Citation:

Wang, F., J. Wang, C. Guan, Q. Ma, and D. Zhang (2016), Mooring observations of equatorial currents in the upper 1000 m of the western Pacific Ocean during 2014, *J. Geophys. Res. Oceans*, 121, 3730–3740, doi:10.1002/2015JC011510.

Received 28 NOV 2015

Accepted 5 MAY 2016

Accepted article online 9 MAY 2016

Published online 2 JUN 2016

<sup>1</sup>Key Laboratory of Ocean Circulation and Waves, Institute of Oceanology, Chinese Academy of Sciences, Qingdao, China, <sup>2</sup>Laboratory for Ocean and Climate Dynamics, Qingdao National Laboratory for Marine Science and Technology, Qingdao, China, <sup>3</sup>University of Chinese Academy of Sciences, Beijing, China, <sup>4</sup>Joint Institute for the Study of the Atmosphere and Ocean, University of Washington, Seattle, Washington, USA, <sup>5</sup>Pacific Marine and Environmental Laboratory, NOAA, Seattle, Washington, USA

**Abstract** Time-depth variations of the equatorial currents over the upper 1000 m depth in the western Pacific Ocean were directly measured by acoustic Doppler current profiler moorings at 2°N, 140°E and 4.7°N, 140°E during January–August 2014. Intraseasonal variations of the equatorial currents, with periods of 37–73 days, were observed encompassing the North Equatorial Countercurrent (NECC), northern branch of the South Equatorial Current (SEC), Equatorial Undercurrent (EUC), Equatorial Intermediate Current (EIC), North Intermediate Countercurrent (NICC), and North Equatorial Subsurface Current (NESC). Compared with previous studies based mainly on shipboard synoptic surveys, the 8-month time series of velocity profiles provided direct evidence for the existence of NESC, captured reversals of the EIC in May and the NESC in June from westward to eastward direction, and revealed larger vertical extensions of the SEC and NESC and greater depths of the EIC and NICC than previously thought. According to a global analysis product of ocean surface current, during January–April 2014, the NECC was located around its southernmost position and with its the weakest intensity over the past 20 years. Some of the anomalous characteristics of these flows may be related to the fickle El Niño of 2014.

## 1. Introduction

Variability of the equatorial currents plays an important role in the mass, heat, and freshwater distribution of the Pacific Ocean, including displacing the western Pacific (WP) warm pool in the east-west direction. Such displacements and associated shifts in the patterns of air-sea interactions are key factors in modulating the evolution of the El Niño/Southern Oscillation (ENSO). Ocean and coupled climate models must therefore faithfully reproduce the zonal transports of these currents in order to accurately simulate ENSO. However, most of our knowledge about these currents is based on synoptic shipboard surveys, which are prone to aliasing by high-frequency variability. Indeed, the few available long-term moored current measurements often revealed surprisingly strong high-frequency variability in the equatorial Pacific.

The vertical structure of zonal currents, packed in a narrow meridional band of the western equatorial Pacific near 140°E, is sketched in Figure 1, based on previous observations and recent updates as summarized below. Among these currents, the mean position and strength of the North Equatorial Countercurrent (NECC), and its seasonal variations are most thoroughly studied based on shipboard and lowered acoustic Doppler current profilers (S-ADCP and L-ADCP), surface drifters, and satellite data [e.g., Johnson *et al.*, 2002; Hsin and Qiu, 2012; Zhao *et al.*, 2013a, 2013b]. The NECC flows eastward between 2°N and 10°N with main axis west of dateline reaching its northernmost position during February–March. The NECC transport is smaller in winter-spring (boreal, same hereafter) and larger in summer-fall. Despite past efforts, overall time-depth measurements of the NECC are lacking, and its intraseasonal variability (ISV) is not well understood. Through analyzing data from the Tropical Atmosphere Ocean (TAO)/Triangle Trans-Ocean Buoy Network (TRITON), Kuroda [2000] found that the New Guinea Coastal Current (NGCC) flows eastward with the northwesterly monsoonal winds in winter and westward with the southeasterly winds in summer. A similar seasonal cycle was revealed from an ocean assimilation dataset based on the GFDL MOM3 model and NODC XBT data [Wang *et al.*, 2002]. The most comprehensive descriptions of the properties and variations of the northern branch of the South Equatorial Current (SEC) and the Equatorial Undercurrent (EUC) to date were

© 2016. The Authors.

This is an open access article under the terms of the Creative Commons Attribution-NonCommercial-NoDerivs License, which permits use and distribution in any medium, provided the original work is properly cited, the use is non-commercial and no modifications or adaptations are made.

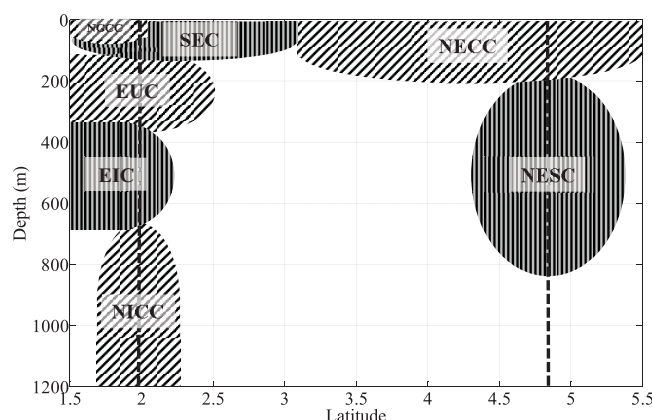


**Figure 1.** A schematic of the structure of the equatorial currents in the western Pacific Ocean near 140°E. Right-upward-slanting and vertical lines denote eastward and westward flows, respectively. Dashed vertical lines denote the latitudes of two subsurface moorings.

based on S-ADCP measurements by Johnson *et al.* [2002]. These authors reported that the SEC is centered at 1°N in the west. Its lower bound lies at about 70 m and reaches its shallowest position during May–June. SEC transport in the WP is much weaker than in the central and eastern Pacific, with a peak in December and a trough in July. The eastward-flowing EUC in the west is displaced to the north of the equator by the New Guinea Coastal Undercurrent (NGCUC), the water from which is also the main source to feed the EUC [Lindstrom *et al.*, 1987; Tsuchiya *et al.*, 1989; Grenier *et al.*, 2011]. Based on S-ADCP measurements, the core of the mean EUC was identified at 0.5°N at 142°E by Gouriou and Toole [1993] but around 2°N at 143°E by Johnson *et al.* [2002]. This disagreement may be a consequence of observations being made in different years or of different averaging time periods. The EUC reaches its shallowest depth and largest transport in summer, and deepest depth and smallest transport in winter.

The Equatorial Intermediate Current (EIC) was studied using S-ADCP and L-ADCP transects [Gouriou and Toole, 1993; Johnson *et al.*, 2002; Marin *et al.*, 2010]. The mean westward-flowing EIC lies at 250–500 m between 2°S and 2°N near 165°E but seasonally reverses into an eastward current. However, in situ measurements are still too sparse to reveal the whole spectrum of EIC variations. Marin *et al.* [2010] combined model simulations and observations to diagnose the EIC, and found that the velocity is westward from July to February and eastward from March to June at 165°E. They suggested that the main mechanism responsible for EIC reversals is the presence of a vertical-propagating Rossby wave, forced by the westward-propagating component of zonal wind stress. The deeper jet, i.e., the North Intermediate Countercurrent (NICC), has rarely been measured. The only measurements that provided a glimpse of this current were made by acoustic dropsonde profilers [Firing, 1987], L-ADCP [Firing *et al.*, 1998], and drifts of ARGO floats at their parking depth [Cravatte *et al.*, 2012]. The NICC is centered at around 1.5°N–2°N and extends from about 500 to 1000 m. It is stronger ( $\sim 8 \text{ cm s}^{-1}$ ) and slightly farther north in the WP than in the central and eastern Pacific. The westward-flowing North Equatorial Subsurface Current (NESC) underneath the NECC has only recently been proposed by Yuan *et al.* [2014] based on absolute geostrophic calculations. The NESC is located between 3°N and 7°N over 200–600 m with a mean velocity of  $2 \text{ cm s}^{-1}$  at 140°E.

Overall, our understanding of the equatorial currents in the WP, especially for those below 300 m, remains fragmentary. Observations with better spatial and temporal coverage are required to draw robust conclusions on the nature of these strong reversing zonal currents packed and stacked in a water column within the narrow equatorial wave guide. Instabilities, meanders, and limitation of geostrophic calculation at low latitude further complicate the interpretation of the limited data obtained so far. Direct measurements by moored ADCPs will no doubt make great contributions to a more complete understanding of these currents. The TAO/TRITON program maintains a few moorings with subsurface current measurements in the WP. However, their moorings are mainly deployed on the equator and are equipped with only one upward-facing ADCP to measure the upper 200–300 m. Addressing the lack of deep velocity observation in the WP, we deployed two subsurface moorings near the core of the EUC and NECC at 140°E in January 2014. Two ADCPs on each mooring continuously measured velocity profiles over the upper 1000 m for the first time in this region.

This study builds on the analysis of the direct current measurements from these two moorings. In addition, with the help of model and satellite data, we describe in detail the characteristics of the observed currents, including their strengths, structures, and intraseasonal to seasonal variability. The analysis reveals some new features of the equatorial currents in the WP.

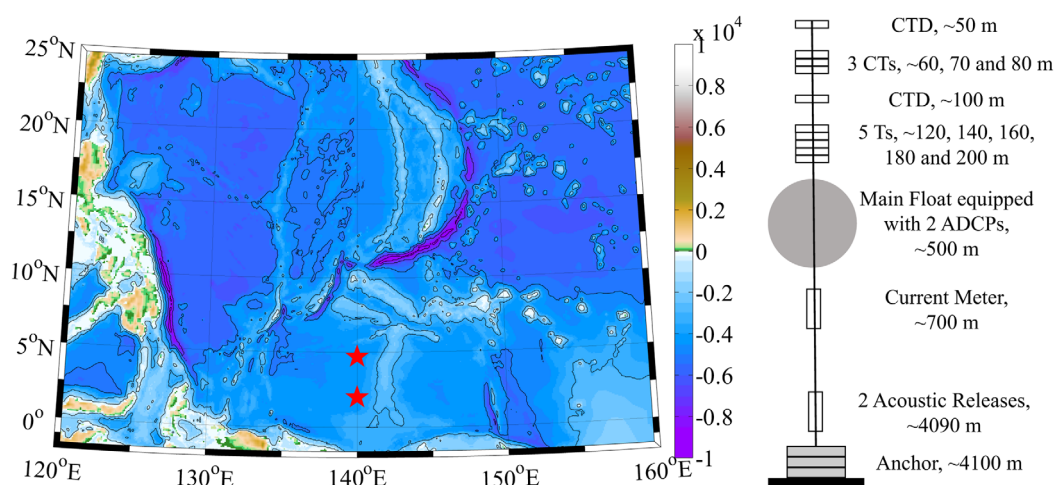


**Figure 2.** (left) Map of topography near mooring sites of 2°N, 140°E, and 4.7°N, 140°E denoted by red stars. (right) Simplified schematic diagram (not at exact scale) of the configuration of two subsurface moorings.

## 2. Data and Methods

### 2.1. Moored ADCPs

One of the subsurface moorings was deployed at 2°N, 140°E on 7 January 2014 and retrieved on 20 August 2014; the other was deployed at 4.7°N, 140°E on 5 January 2014 and retrieved on 21 August 2014 (Figure 2). Both moorings had the same configuration: one upward-looking and one downward-looking TRDI 75 kHz ADCPs were mounted on the main float at ~500 m. The mooring also supported other instruments, including one TRDI DVS current meter, two SBE 37 conductivity-temperature-depth (CTDs), three SBE 37 conductivity-temperature (CTs), and five SBE 56 temperature sensors (Ts, Figure 2).

The ADCPs returned the velocity profiles over the depth range of 50–1050 m with a vertical bin size of 8 m. Each velocity profile was derived by averaging 35 pings over 1 h. The velocity data were interpolated vertically to standard depth of 1 m interval and then averaged to derive the daily mean. To remove the tidal effect, a central 3 day running mean was applied to the daily data.

### 2.2. HYCOM, AVISO, and OSCAR

Outputs from the global HYCOM (Hybrid Coordinate Ocean Model) consortium were downloaded from <http://hycom.org>. The model was configured on a Mercator grid with a horizontal resolution of  $1/12^\circ$  in longitude/latitude. The vertical resolution varies from 10 m near the surface to 500 m near the bottom, with a total of 32 layers. Daily outputs over the period 1995–2012 were obtained from the reanalysis run while those over the period 2013–2014 were obtained from the real-time analysis run.

AVISO (Archiving, Validation, and Interpretation of Satellite Oceanographic) gridded sea surface height (SSH) data with a resolution of  $1/4^\circ$  in longitude/latitude were also used to aid interpretation of our observations. This product merges SSH measurements from the Saral/Altika, Cryosat-2, Jason-2, and Haiyang-2A satellite altimeters. The AVISO SSH data were obtained from <http://motu.aviso.oceanobs.com/>. Daily fields over January–August 2014 are analyzed.

The OSCAR (Ocean Surface Current Analyses Real time) data were used to depict the surface currents in the whole WP. The OSCAR surface currents, representing the vertical average of the top 30 m, are calculated from altimeter-based SSH, sea surface winds, and sea surface temperature on global grid of  $1/3^\circ$  every ~5 days. We obtained the OSCAR data through the website: <http://www.oscar.noaa.gov/>. The output during 1995–2014 is used in this study.

### 2.3. Main Axis and Intensity of Zonal Currents

In the following, the latitudes of the axis of zonal currents in HYCOM and OSCAR are evaluated using the concept of “center of volume transport” [Hsin and Qiu, 2012]:

$$Y(x, t) = \frac{\int_{Y_S}^{Y_N} y \cdot U(x, y, t) dy}{\int_{Y_S}^{Y_N} U(x, y, t) dy}, \quad (1)$$

where  $U$  is the zonal velocity,  $Y$  denotes the latitude in degrees, and  $Y_N$  and  $Y_S$  are the northern and southern limits of integration, respectively. To calculate the NECC main axis ( $Y_{NECC}$ ), 10°N and 2°N are adopted as  $Y_N$  and  $Y_S$ , and to calculate the EUC main axis ( $Y_{EUC}$ ), 2.5°N and 1°S are adopted as  $Y_N$  and  $Y_S$ .

The intensity (INT) of a current is defined as the water volume being transported, written as

$$INT(x, t) = \int_{Y_S}^{Y_N} U(x, y, t) dy. \quad (2)$$

$Y_N$  and  $Y_S$  are set to  $Y_{NECC} + 4^\circ$  and the larger value of  $Y_{NECC} - 4^\circ$  and  $2^\circ$  for the NECC intensity ( $INT_{NECC}$ ).  $Y_N$  and  $Y_S$  are set to 2.5°N and 1°S for the EUC intensity ( $INT_{EUC}$ ).

### 3. Results

#### 3.1. Surface Currents

Figure 3 shows the time-depth variations of daily zonal currents ( $U$ ) observed by the moored ADCPs and their corresponding energy spectra. To complement our point measurements at the two locations, the HYCOM and OSCAR data are used to understand the latitudinal positions for surface currents relative to the mooring (Figures 4a and 4b). To assess the abilities of HYCOM and OSCAR to simulate the surface currents, we compare their time series of  $U$  with the ADCP measurements. In this evaluation, the layers that represent the surface are different in three datasets. For the mooring and HYCOM, we choose  $U$  at 88 m for 2°N and  $U$  at 71 m for 4.7°N, the top levels of ADCP measurements at the two locations, for the comparison. HYCOM- $U$  at 88 and 71 m are obtained through linear interpolation of modeled depth levels. OSCAR- $U$  represents the mean velocity over the top 30 m. Between the mooring and HYCOM (OSCAR), the correlation coefficients ( $r$ ) are high and significant at the 0.01 level, and the normalized root-mean-square errors (NRMSE) are low, as denoted in Figures 4c and 4d. The NRMSE is defined as:

$$NRMSE = \frac{\sqrt{\frac{1}{n} \sum_{i=1}^n (U_{mooring} - U_{HYCOM(OSCAR)})^2}}{\max(U_{mooring}) - \min(U_{mooring})}, \quad (3)$$

where  $n$  is the number of data values,  $\max(U_{mooring})$  and  $\min(U_{mooring})$  are the maximum and minimum of observed velocities, respectively. This comparison suggests that the variability and magnitude of the HYCOM and OSCAR surface currents are in reasonable agreement with the observations. Therefore, the HYCOM and OSCAR outputs will be used to illustrate the structures and variations of surface currents.

There are multiple velocity cores coherent over extended depth ranges in the time-depth diagrams of Figure 3, indicating significant ISV. To obtain the period and intensity of ISVs, we calculate the energy spectral density of the daily zonal current anomaly after applying a 20–90 day band-pass filter.

##### 3.1.1. SEC and NGCC

For the mooring at 2°N,  $U$  above 80 m was unfortunately not sampled by the upward-looking ADCP. Between 80 and 200 m,  $U$  was westward during 9 January to 9 March and 26 April to 13 July, and eastward during the rest of the measurement period (Figure 3). The HYCOM and OSCAR data (Figures 4a and 4b) suggest that the westward current was part of the SEC. The lower bound of the SEC lay at about 140 m depth before March and then deepened to 200 m in May–June (Figure 3). The vertical extent of the SEC is about 80 m larger than reported previously [e.g., Johnson et al., 2002].

The observed eastward current above 100 m before April (Figure 3) represents the northern edge of NGCC as evidenced by the HYCOM and OSCAR data (Figures 4a and 4b). The HYCOM and OSCAR outputs show that the seasonal reversal of the NGCC persisted from January until late April in 2014, longer than in previous findings [Kuroda, 2000]. After April, the observed eastward current above 100 m appears to be part of the NECC, a consequence of a southward shift of the NECC main axis ( $Y_{NECC}$ ) (Figures 4a and 4b). In late June, the NECC limited the SEC to the subsurface at the mooring location.



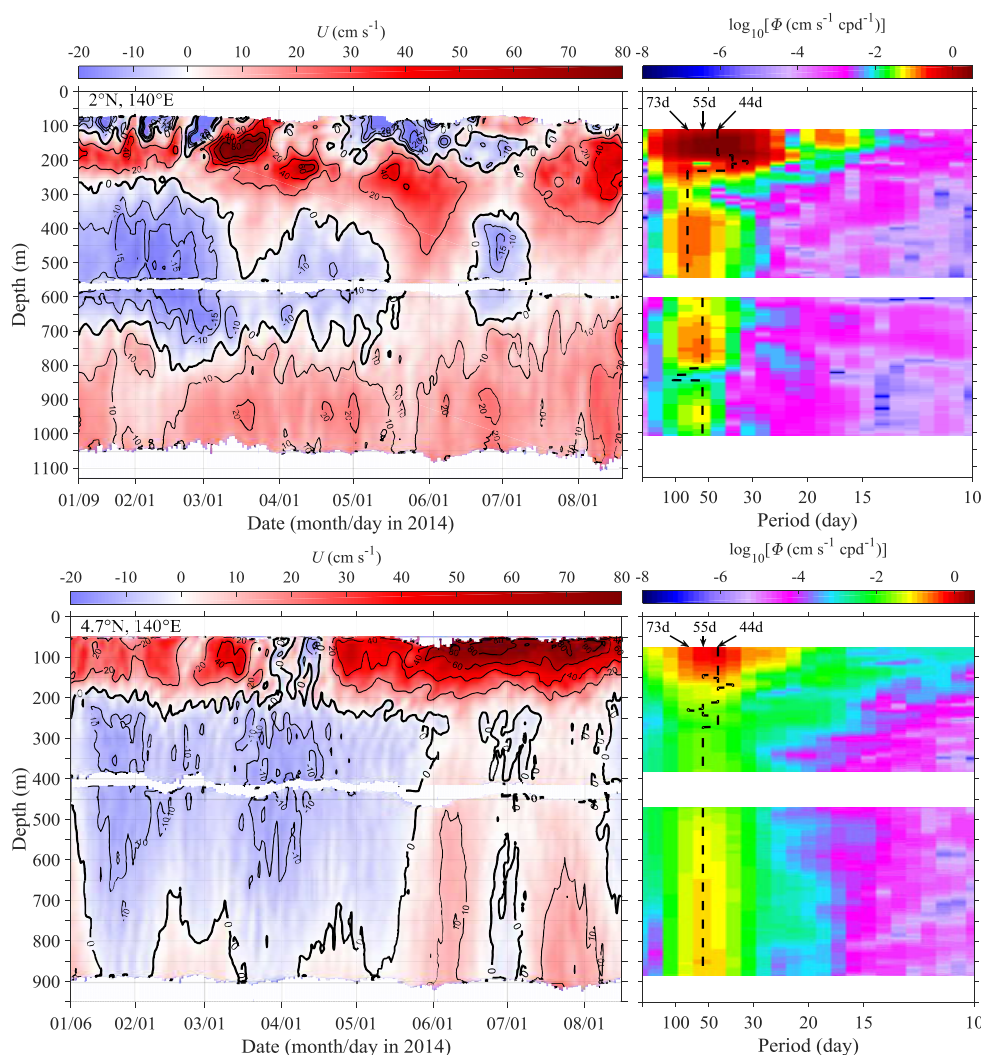


**Figure 3.** (left) Time-depth variations of daily zonal currents observed by moored ADCPs. (right) Vertical distributions of energy spectra of 20–90 day band-pass filtered daily zonal currents. Dash vertical lines mark the spectral peak at each depth. Top and bottom plots show results for moorings at 2°N and 4.7°N, respectively.

### 3.1.2. NECC

For the mooring at 4.7°N,  $U$  above about 200 m was eastward, representing the NECC. In terms of seasonality, our observed NECC velocity was smaller in winter-spring and larger in summer, consistent with previous studies [e.g., Gouriou and Toole, 1993]. Its lower depth bound was stable at 200 m.

In both HYCOM and OSCAR,  $Y_{NECC}$  in the surface layer tended to move northward during January–April over the past 20 years (1995–2014) as shown by the green curves in Figures 4a and 4b. The  $Y_{NECC}$  in 2014, however, deviated significantly from this general northward movement and reached nearly its southernmost position over the 20 year period. Notably during 31 March to 17 April, the sudden southward shift of  $Y_{NECC}$  manifested the reversal of the observed surface current. While  $Y_{NECC}$  was attaining its southernmost position, the NECC intensity ( $INT_{NECC}$ ) in the surface layer during January–April 2014 was the weakest over the period 1995–2014 (Figure 4e). Variations in SSH around the NECC were found to be consistent with changes in  $Y_{NECC}$  and  $INT_{NECC}$  [Hsin and Qiu, 2012; Zhao et al., 2013a]. Based on the geostrophic relationship, a decreasing SSH corresponds to anomalous westward (eastward) current on its northern (southern) side and resultant southward shift of  $Y_{NECC}$  and vice versa;  $INT_{NECC}$  is determined by the meridional SSH gradient. We thus examine variations of SSH in the northern (4°N–6°N,  $SSH_N$ ) and southern regions (1°N–3°N,  $SSH_S$ ) relative to the mooring site, and the difference between them ( $\Delta SSH = SSH_S - SSH_N$ ). Before mid-March,  $SSH_N$  and  $SSH_S$  had a general downward trend, and

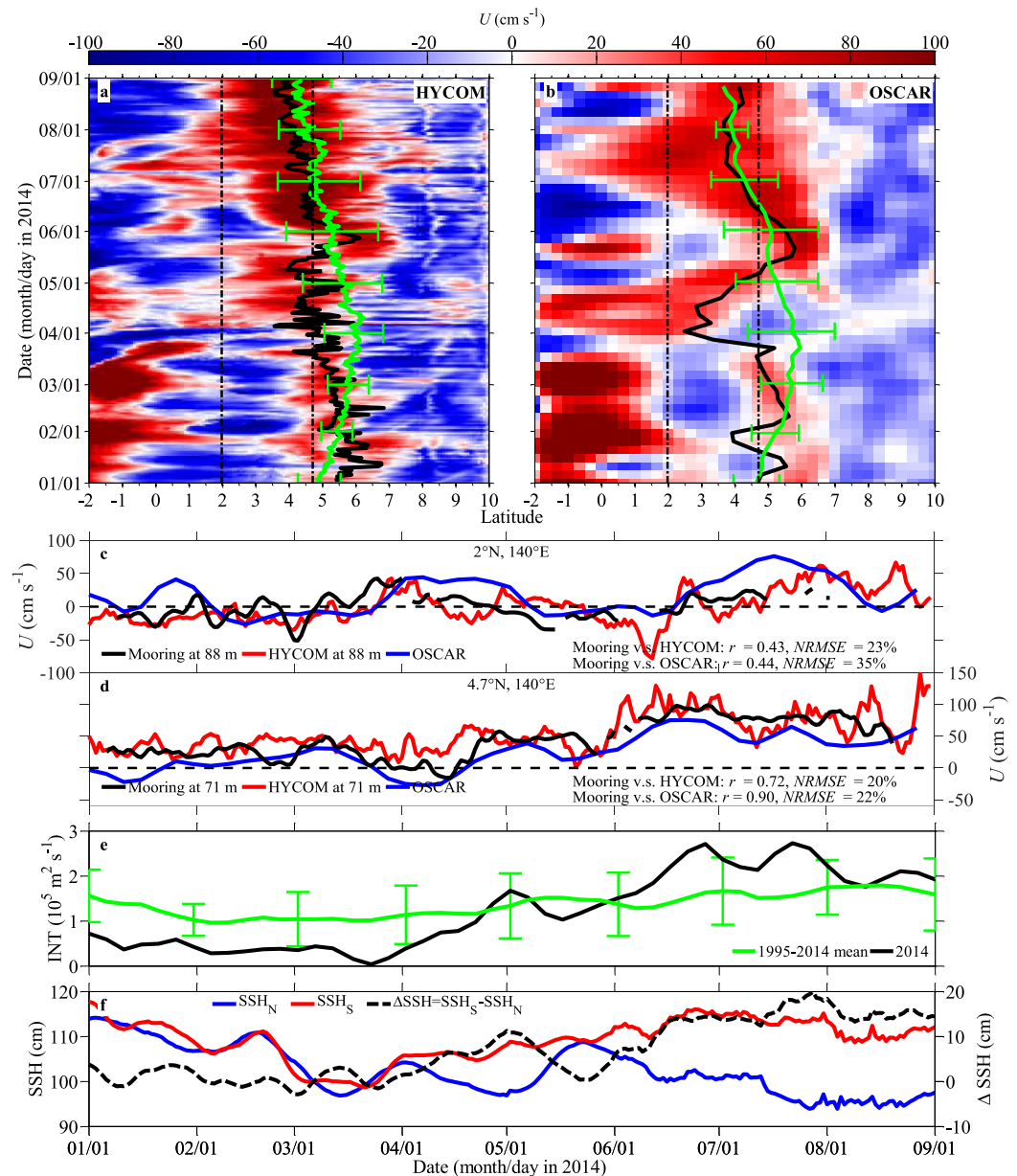


**Figure 4.** (a) HYCOM and (b) OSCAR latitude-time variations of surface zonal currents ( $U$ ). Time variations of  $U$  obtained from mooring, HYCOM, and OSCAR at (c) 2°N and (d) 4.7°N, (e) OSCAR NECC intensity, (f) AVISO SSH<sub>N</sub> in northern (4°N–6°N) and SSH<sub>S</sub> in southern (1°N–3°N) regions relative to the mooring site, and their difference ( $\Delta SSH = SSH_S - SSH_N$ ). The NECC main axis (in Figures 4a and 4b) and intensity (in Figure 4e) in 2014 are denoted by black curves, and the averaging and standard deviation over 1995–2014 are denoted by green curves and bars.

two decreasing events occurred during late January and from mid-February to mid-March. For HYCOM,  $r$  of SSH<sub>N</sub>, SSH<sub>S</sub>, and  $\Delta SSH$  with  $Y_{NECC}$  are 0.68, -0.06, and -0.61, respectively; while  $r$  with  $INT_{NECC}$  are -0.60, 0.53, and 0.87, respectively. For OSCAR,  $r$  of SSH<sub>N</sub>, SSH<sub>S</sub>, and  $\Delta SSH$  with  $Y_{NECC}$  are 0.56, 0, and -0.48, respectively; while  $r$  with  $INT_{NECC}$  are -0.51, 0.68, and 0.91, respectively. Above results suggest that the NECC is approximately in geostrophic balance, and confirm the impacts of SSH<sub>N</sub> on  $Y_{NECC}$  and  $\Delta SSH$  on  $INT_{NECC}$ .

### 3.2. Subsurface Currents

#### 3.2.1. EUC

The eastward flow centered at ~200 m represents the EUC. During the 8-month measurement period, there were five velocity maximums (Figure 3). The intensities of the EUC started out weak in winter (20 cm s<sup>-1</sup>),

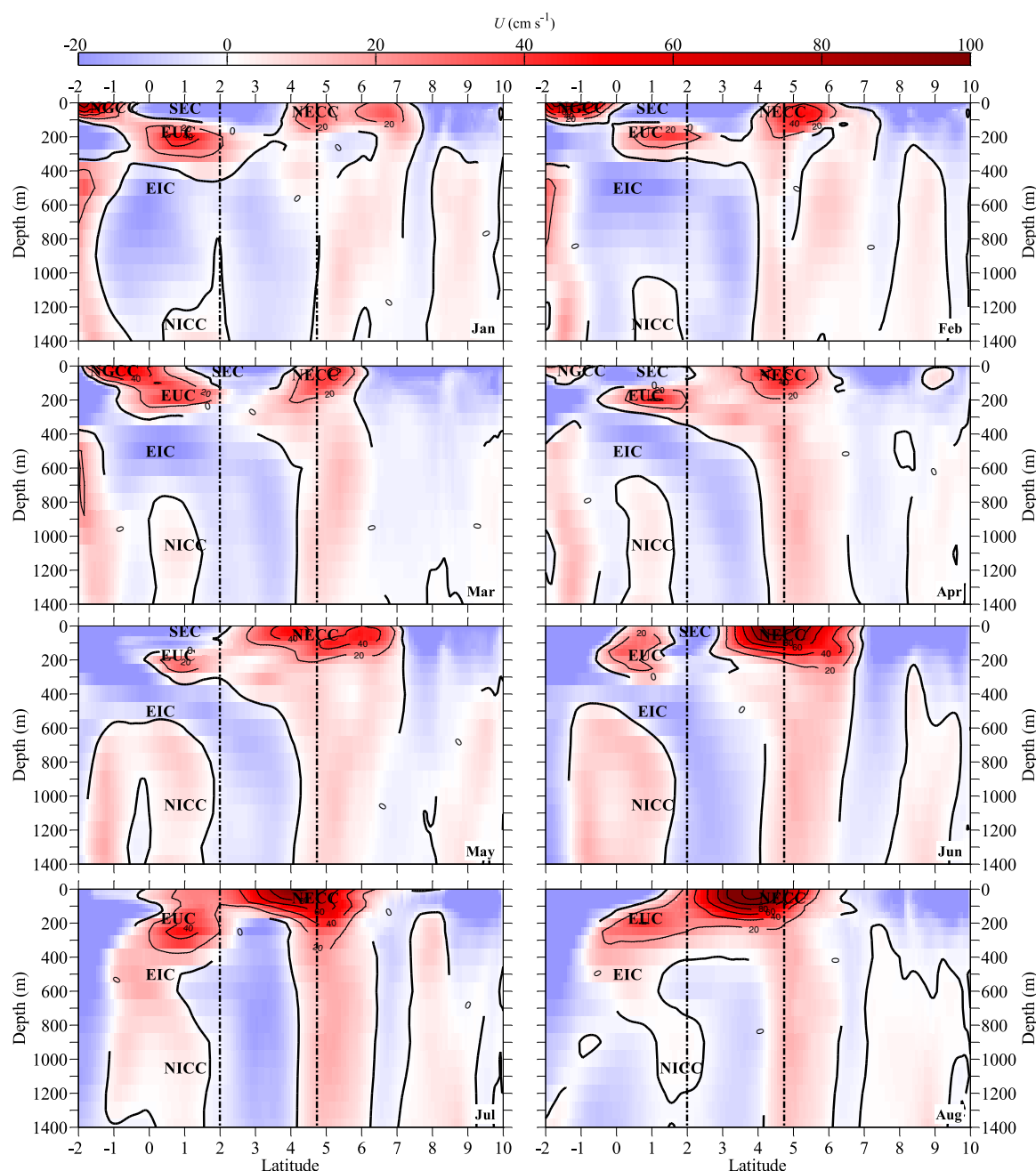


**Figure 5.** Monthly distributions of HYCOM zonal current ( $U$ ) along  $140^{\circ}\text{E}$  during January–August 2014. Dash-dotted lines denote the latitudes of two moorings.

strengthened in March ( $80 \text{ cm s}^{-1}$ ), and fell to  $40 \text{ cm s}^{-1}$  in early April, mid-May, and August. The EUC cores were at 200 m before February, shoaled in March (175 m), deepened around June (300 m), and shoaled again in August (250 m). The shallowest depth associated with the maximum velocity was present in March, 3 months earlier than reported by *Johnson et al.* [2002]. The period of the EUC's ISV varied from 37 to 73 days.

Next, we compare the observed EUC with that simulated by HYCOM. The monthly distributions of HYCOM zonal currents during the observing period are depicted in Figure 5. In this analysis, the EUC is defined as the 100–300 m mean eastward flow. We calculate the correlation and *NRMSE* of the EUC obtained from the HYCOM outputs at different latitudes between  $1^{\circ}\text{S}$  and  $2.5^{\circ}\text{N}$  and that from the mooring. At  $2^{\circ}\text{N}$ , the correlation ( $r = 0.03$ ) is poor due to their evident time lapse (Figure 6a). However, the time-lag between the

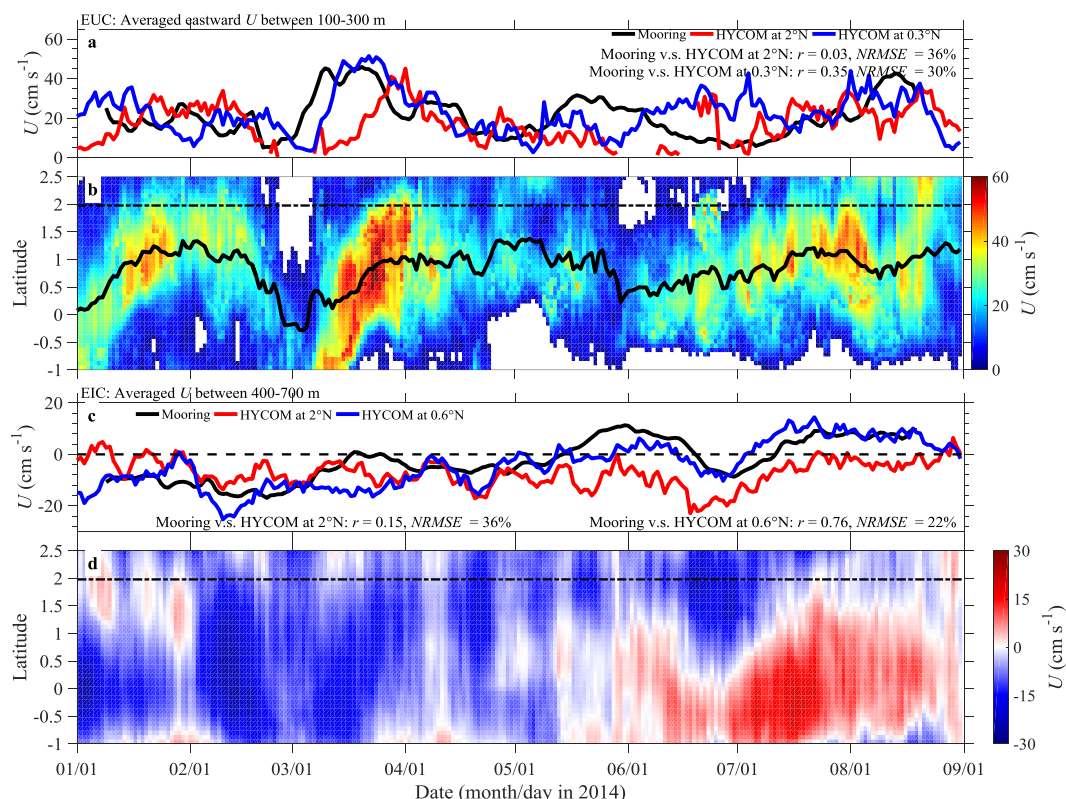


**Figure 6.** EUC: (a) time series of eastward current ( $U$ ) averaged over 100–300 m from mooring (black) and HYCOM (red and blue); (b) latitude-time variations of  $U$  from HYCOM averaged over 100–300 m with solid curve denoting the EUC main axis. EIC: (c) and (d) same as Figures 6a and 6b but for  $U$  averaged over 400–700 m. Dash-dotted lines in Figures 6b and 6d denote the latitudes of moorings.

HYCOM outputs at the southern sites and the mooring measurements is smaller. It is found that the HYCOM output at 0.3°N is most highly correlated with the mooring observations ( $r = 0.35$ ), and the  $NRMSE$  (30%) is the smallest. Although the simulated EUC seems to be shifted southward or has a phase shift compared to observation [also see Johnson *et al.*, 2002], the HYCOM captures the general variation and magnitude of the EUC, and can provide some useful information about the observed EUC variability at the mooring location (Figure 6b).

Both the HYCOM EUC main axis ( $Y_{EUC}$ ) and intensity ( $INT_{EUC}$ ) vary significantly. Their ISVs had the same period of 55 days (figure not shown). The strong ISV of the observed EUC was related to the migration of  $Y_{EUC}$  and the variation of  $INT_{EUC}$ . Increasing  $INT_{EUC}$  and northward migration of  $Y_{EUC}$  were consistent with the observed maximum velocity in March.

### 3.2.2. EIC

Underneath the EUC, the observed westward flow between 300 and 800 m depth is a part of the EIC (Figure 3). The upper bound of westward EIC was at 300 m during January–February, and then deepened to 400 m in April; its lower bound was at 700 m except in late February when it deepened to 800 m. EIC mean depth is 100–200 m deeper than the previous result at 165°E [Marin *et al.*, 2010], consistent with the westward deepening tendency [Johnson *et al.*, 2002]. The velocity of westward EIC averaged between 400 and 700 m increased from January to February, then decreased in March, and slightly rebounded from mid-April to mid-May (Figure 6c). As time went on, a striking feature at this same depth range was the current reversal. An eastward flow emerged from mid-May to mid-June and then from mid-July to the end of measurement. The longitude-time variation of the EIC was summarized from various cruises and model results by Marin *et al.* [2010, Figure 8]. They showed that the timing of the reversal increases westward from January at 140°W to April–May at 165°E, and then to May at 140°E where our mooring was located. This westward phase propagation of the EIC reversal is related to the vertical propagation of an annual Rossby wave forced by the westward-propagating component of the annual equatorial zonal wind stress. However, the period of eastward current in our observation lasted for at least two months, much longer than the results of Marin *et al.* [2010] based on shipboard synoptic surveys and model simulations.



We further interpret our observations with HYCOM for the EIC defined as the mean flow between 400 and 700 m (Figure 6d). We compared the observed EIC with the HYCOM EIC at different latitudes between 1°S and 2.5°N. Mooring-model correlation is weak ( $r = 0.15$ ) at 2°N, and highest ( $r = 0.76$ ) with smallest *NRMSE* (22%) at 0.6°N (Figure 6c). Notably, HYCOM captures the time evolution of the EIC, especially its reversal. From the whole picture provided by HYCOM (Figure 5), the EIC reversed to be eastward only from July to August; during the period from mid-May to mid-June, the shoaling of the eastward NICC led to the decrease in the depth range of the EIC, and eastward current between 400 and 700 m in the northern hemisphere of Figure 6d. HYCOM cannot give a robust explanation to the first observed eastward period, but suggests that the second observed eastward period is associated with the EIC's reversal. Besides the seasonal variability, the EIC also had strong ISV with a period of 73 days (Figure 3), longer than those of other observed currents. The variations of current intensity and axis both contribute to the ISV of the observed EIC.

### 3.2.3. NICC

The deepest eastward current observed by moored ADCP at 2°N is the NICC. Its vertical distribution, however, was not fully resolved. The depth range of the NICC started at 700 m and ended deeper than 1050 m. Our observed depth is 200 m deeper than reported by *Firing et al.* [1998]. The time-depth-mean NICC- $U$  is  $12 \text{ cm s}^{-1}$ . Several velocity cores with  $U$  larger than  $20 \text{ cm s}^{-1}$  were observed at  $\sim 950 \text{ m}$ , indicating ISV of the NICC at a period of  $\sim 55$  days (Figure 3). The intensity of its ISV is weak compared to that of other currents.

The observed NICC is compared with the HYCOM simulation. In HYCOM, the NICC and the South Intermediate Countercurrent (SICC) are denoted by the two eastward currents below 500 m on both sides of the equator (Figure 5). Modeled NICC is generally located between the equator and 2°N, further south compared to our observations. Note that in HYCOM, the EUC is also displaced further south compared to our own observations and *Johnson et al.* [2002]. The upper bound of the NICC was stable at 700 m in our measurements, but varied over a large depth range of 600–1200 m in HYCOM. The observed NICC was clearly present throughout the measurement period with a mean velocity of  $12 \text{ cm s}^{-1}$ , reaching a maximum speed of  $30 \text{ cm s}^{-1}$  in August, whereas in HYCOM, the NICC almost disappeared in August, and the mean velocity was only  $4 \text{ cm s}^{-1}$ . The HYCOM solution shows significant discrepancy with the observed NICC in terms of its latitudinal and depth locations, mean magnitude, and time variability.

### 3.2.4. NESC

Between 200 and 900 m, a westward flow was observed before June and the flow reversed into an eastward current afterward. The westward current is the NESC, the first direct evidence of its existence and time-depth variation. In comparison with previous findings based on absolute geostrophic calculations [*Yuan et al.*, 2014], the observed depth range is much larger and the time-depth mean velocity of  $4.8 \text{ cm s}^{-1}$  is stronger. Similar to the reversals of the EIC, the direction shift of the NESC after June may also be related to vertical propagation of surface forced Rossby waves or the manifestations of subthermocline eddies. More detailed investigation of the mechanisms responsible in NESC's variability will be pursued in a separate study. The ISV of the NESC had a period of 55 days (Figure 3). HYCOM (Figure 5) fails to reproduce the NESC under the NECC but rather simulates a westward flow between 2°N and 4°N.

## 4. Discussion

Time-depth variations of equatorial currents over the upper 1000 m depth in the WP were directly measured by two moorings at 2°N, 140°E and 4.7°N, 140°E during January–August 2014. The velocity profiles measured by the moored ADCPs confirmed the basic characteristics of the NECC, SEC, NGCC, EUC, EIC, NICC, and NESC proposed by previous studies, but also revealed some new features about these zonal currents. This is the first time, to our knowledge, that the time-depth variations of EIC, NICC, and NESC were directly observed in this region. The newly observed features from our moored ADCP measurements include the larger vertical extent of the SEC and NESC, and the greater depths of the EIC and NICC. The 8-month time series also captured reversals of the EIC in mid-May and the NESC in early June from westward to eastward direction. Our measurement obtained the direct evidence for the existence of NESC.

The spectra of observed velocities reveal significant ISVs of the NECC, EUC, EIC, NICC, and NESC with periods of 44, 37–73, 73, 55, and 55 days, respectively. With the help of model and satellite data, the observed ISVs of NECC, EUC, and EIC at the mooring locations can be related to variations in their axes and intensities.

Formation of zonal currents in the upper tropical Pacific was related to the structure of wind stress curl contributing to the Sverdrup balance and additional nonlinear advection and friction effects by Kessler *et al.* [2003]. The mechanisms for their ISV, however, strongly depend on their spatial scales. F. W. Wang *et al.* (Intraseasonal Variability of the Surface Zonal Currents in the Western Tropical Pacific Ocean: Characteristics and Mechanisms, manuscript submitted to *Journal of Physical Oceanography*, 2016) found that the primary mechanism for ISV is the influence of internal variability related to mesoscale eddies at local scale ( $<200$  km), and the influence of intraseasonal wind forcing at large scale ( $>500$  km). In the NECC and SEC regions, barotropic instability induced by horizontal shears of flows is the major cause for the mesoscale eddy variability [Zhao *et al.*, 2013a; Chen *et al.*, 2015]. For intermediate currents, they are suggested to arise from the rectification of deep equatorial intraseasonal variability [Hua *et al.*, 2008; Ascani *et al.*, 2010]. Currently, there are two hypotheses for the source of deep equatorial intraseasonal variability: one is instability of the deep western boundary current crossing the equator [d'Orgeville *et al.*, 2007; Ménesguen *et al.*, 2009]; the other is instability of the wind-driven upper ocean currents (such as tropical instability waves) [Ascani *et al.*, 2015; Matthießen *et al.*, 2015]. The relevance of the proposed mechanisms to the present observations merits further study.

Variation of the WP warm pool modulates the development of El Niño–Southern Oscillation. Two relatively strong westerly wind events (WWEs) in late January–March 2014 hinted the initiation of El Niño. However, the absence of WWEs and the redevelopment of easterly wind anomalies after mid-2014 appear to have quenched the highly anticipated El Niño (Menkes *et al.*'s [2014] Figure 2 shows the time variation of wind stress). As the measurement period of moorings coincides with the fickle growth of El Niño in 2014, it is interesting to muse about our observation in this context. As previously discussed, the weakening and reversing episodes of the NECC at 4.7°N during January–April, and the episode of eastward flow in April at 2°N were observed by the two moorings. Based on comparative analysis of the OSCAR data, these variations were associated with a southward shift of the NECC and an unusually persisting eastward NGCC, respectively. Furthermore, during January–April 2014, the NECC was almost at its southernmost position and weakest over the past 20 years, consistent with SSH decreasing events between 1°N and 6°N (Figure 4f). Note that the SSH decreasing events coincided with the two WWEs. This can be understood in the following. WWEs produce meridional gradient of zonal wind stress, and result in the upwelling Ekman pumping and the diminishing SSH off the equator in the northern hemisphere. We speculate that longer persisting eastward NGCC and the enhanced EUC (stronger EUC generally corresponds to La Niña, however) [Johnson *et al.*, 2002] in early March observed by the mooring at 2°N are also related to WWEs. Besides an equatorial downwelling Kelvin wave [Menkes *et al.*, 2014], more anomalous features of the NECC, NGCC, and EUC are found during periods of WWEs. Further understanding the linkages of the intraseasonal and seasonal variations of equatorial currents with the WWEs and the fickle El Niño in 2014 could shed new light on the coupled climate dynamics in the equatorial Pacific.

# Acknowledgments

We thank the anonymous reviewer for encouragement and very helpful comments and suggestions. The crew of R/V Kexue (Science) is thanked for their assistance with the deployment and retrieval of two subsurface moorings. This study is supported by the National Basic Research Program of China (grant 2012CB417401), the National Natural Science Foundation of China (grant 41406015, 41421005, and U1406401), and the Strategic Priority Research Program of the Chinese Academy of Sciences (grant XDA11010204). The mooring data used here can be accessed freely for research purpose upon request to Fan Wang (fwang@qdio.ac.cn). Fan Wang and Jianing Wang contributed equally to this work.

# References

- Ascani, F., E. Firing, P. Dutrieux, J. P. McCreary, and A. Ishida (2010), Deep equatorial ocean circulation induced by a forced dissipated Yanai beam, *J. Phys. Oceanogr.*, *40*, 1118–1142.
- Ascani, F., E. Firing, J. P. McCreary, P. Brandt, and R. J. Greatbatch (2015), The deep equatorial ocean circulation in wind-forced numerical solutions, *J. Phys. Oceanogr.*, *45*, 1709–1734.
- Chen, X., B. Qiu, S. Chen, Y. Qi, and Y. Du (2015), Seasonal eddy kinetic energy modulations along the North Equatorial Countercurrent in the western Pacific, *J. Geophys. Res. Oceans*, *120*, 6351–6362, doi:10.1002/2015JC011054.
- Cravatte, S., W. S. Kessler, and F. Marin (2012), Intermediate zonal jets in the tropical Pacific Ocean observed by Argo floats, *J. Phys. Oceanogr.*, *42*, 1475–1485.
- d'Orgeville, M., B. L. Hua, and H. Sasaki (2007), Equatorial deep jets triggered by a large vertical scale variability within the western boundary layer, *J. Mar. Res.*, *65*, 1–25.
- Firing, E. (1987), Deep zonal currents in the central equatorial Pacific, *J. Mar. Res.*, *45*, 791–812.
- Firing, E., S. E. Wijffels, and P. Hacker (1998), Equatorial subthermocline currents across the Pacific, *J. Geophys. Res.*, *103*, 21,413–21,423.
- Gouriou, Y., and J. Toole (1993), Mean circulation of the upper layers of the western equatorial Pacific Ocean, *J. Geophys. Res.*, *98*, 22,495–22,520.
- Grenier, M., S. Cravatte, B. Blanke, C. Menkes, A. Koch-Larrouy, F. Durand, A. Melet, and C. Jeandel (2011), From the western boundary currents to the Pacific Equatorial Undercurrent: Modeled pathways and water mass evolutions, *J. Geophys. Res.*, *116*, C12044, doi:10.1029/2011JC007477.
- Hsin, Y.-C., and B. Qiu (2012), Seasonal fluctuations of the surface North Equatorial Countercurrent (NECC) across the Pacific basin, *J. Geophys. Res.*, *117*, C06001, doi:10.1029/2011JC007794.
- Hua, B. L., M. d'Orgeville, M. D. Fruman, C. Ménesguen, R. Schopp, P. Klein, and H. Sasaki (2008), Destabilization of mixed Rossby gravity waves and the formation of equatorial zonal jets, *J. Fluid Mech.*, *610*, 311–341.
- Johnson, G. C., B. M. Sloyan, W. S. Kessler, and K. E. McTaggart (2002), Direct measurements of upper ocean currents and water properties across the tropical Pacific during the 1990s, *Prog. Oceanogr.*, *52*, 31–61.

- Kessler, W. S., G. C. Johnson, and D. W. Moore (2003), Sverdrup and Nonlinear Dynamics of the Pacific Equatorial Currents, *J. Phys. Oceanogr.*, **33**, 994–1008.
- Kuroda, Y. (2000), Variability of currents off the northern coast of New Guinea, *J. Phys. Oceanogr.*, **56**, 103–116.
- Lindstrom, E., R. Lukas, R. Fine, E. Firing, S. Godfrey, G. Meyers, and M. Tsuchiya (1987), The western equatorial Pacific Ocean circulation study, *Nature*, **330**, 533–537.
- Marin, F., E. Kestenare, T. Delcroix, F. Durand, S. Cravatte, G. Eldin, and R. Bourdallé-Badie (2010), Annual reversal of the Equatorial Intermediate Current in the Pacific: Observations and model diagnostics, *J. Phys. Oceanogr.*, **40**, 915–933.
- Matthießen, J.-D., R. Greatbatch, P. Brandt, M. Claus, and S.-H. Didwischus (2015), Influence of the equatorial deep jets on the north equatorial countercurrent, *Ocean Dyn.*, **65**, 1095–1102.
- Ménèsgruen, C., B. L. Hua, M. D. Fruman, and R. Schopp (2009), Dynamics of the combined extra-equatorial and equatorial deep jets in the Atlantic, *J. Mar. Res.*, **67**, 323–346.
- Menkes, C. E., M. Lengaigne, J. Vialard, M. Puy, P. Marchesiello, S. Cravatte, and G. Cambon (2014), About the role of Westerly Wind Events in the possible development of an El Niño in 2014, *Geophys. Res. Lett.*, **41**, 6476–6483, doi:10.1002/2014GL061186.
- Tsuchiya, M., R. Lukas, R. A. Fine, E. Firing, and E. Lindstrom (1989), Source waters of the Pacific Equatorial Undercurrent, *Prog. Oceanogr.*, **23**, 101–147.
- Wang, F., P. Chang, D. Hu, and H. Seidel (2002), Circulation in the western tropical Pacific Ocean and its seasonal variation, *Chin. Sci. Bull.*, **47**, 591–595.
- Yuan, D., Z. Zhang, P. C. Chu, and W. K. Dewar (2014), Geostrophic circulation in the tropical north Pacific Ocean based on Argo profiles, *J. Phys. Oceanogr.*, **44**, 558–575.
- Zhao, J., Y. Li, and F. Wang (2013a), Dynamical responses of the west Pacific North Equatorial Countercurrent (NECC) system to El Niño events, *J. Geophys. Res.*, **118**, 2828–2844, doi:10.1002/jgrc.20196.
- Zhao, J., Y. Li, and F. Wang (2013b), The role of mindanao dome in the variability of the Pacific North equatorial current bifurcation, *J. Oceanogr.*, **69**, 313–327.